micromachines

MDPI

Article

Construction of a CQDs/Ag_3PO_4/$BiPO_4$ Heterostructure Photocatalyst with Enhanced Photocatalytic Degradation of Rhodamine B under Simulated Solar Irradiation

Huajing Gao [1,3], Chengxiang Zheng [1], Hua Yang [1,*], Xiaowei Niu [3] and Shifa Wang [2,3,*]

1 State Key Laboratory of Advanced Processing and Recycling of Non-Ferrous Metals, Lanzhou University of Technology, Lanzhou 730050, China
2 Chongqing Key Laboratory of Geological Environment Monitoring and Disaster Early-Warning in Three Gorges Reservoir Area, Chongqing Three Gorges University, Chongqing 404000, China
3 School of Electronic and Information Engineering, Chongqing Three Gorges University, Chongqing 404000, China
* Correspondence: hyang@lut.cn (H.Y.); 20180011@sanxiau.edu.cn (S.W.); Tel.: +86-931-2973783 (H.Y.); +86-931-13619399839 (S.W.)

Received: 4 July 2019; Accepted: 21 August 2019; Published: 23 August 2019

Abstract: A carbon quantum dot (CQDs)/Ag_3PO_4/$BiPO_4$ heterostructure photocatalyst was constructed by a simple hydrothermal synthesis method. The as-prepared CQDs/Ag_3PO_4/$BiPO_4$ photocatalyst has been characterized in detail by X-ray diffraction, field-emission scanning electron microscopy, transmission electron microscopy, X-ray photoelectron spectroscopy, ultraviolet–visible spectroscopy, and photoelectrochemical measurements. It is demonstrated that the CQDs/Ag_3PO_4/$BiPO_4$ composite is constructed by assembling Ag_3PO_4 fine particles and CQDs on the surface of rice-like $BiPO_4$ granules. The CQDs/Ag_3PO_4/$BiPO_4$ heterostructure photocatalyst exhibits a higher photocatalytic activity for the degradation of the rhodamine B dye than that of Ag_3PO_4, $BiPO_4$, and Ag_3PO_4/$BiPO_4$. The synergistic effects of light absorption capacity, band edge position, separation, and utilization efficiency of photogenerated carriers play the key role for the enhanced photodegradation of the rhodamine B dye.

Keywords: carbon quantum dots; CQDs/Ag_3PO_4/$BiPO_4$; photodegradation activity; synergistic effect; photocatalytic mechanism

1. Introduction

The photocatalytic degradation of organic pollutants in wastewater is an attractive, environmentally friendly and green method that offers a way to harness solar power efficiently and convert them into non-toxic degradation products [1–8]. Recently, although great progress has been made in the field of photocatalysis, only few photocatalysts can effectively use visible light in the degradation of organic pollutions. Therefore, it is desirable to develop novel photocatalysts with high visible-light utilization for degradation of organic pollutions in wastewater. In recent years, silver phosphate (Ag_3PO_4) based composite photocatalysts, such as $Bi_4Ti_3O_{12}$/Ag_3PO_4 [9], Ag_3PO_4/$NaTaO_3$ [10], MoS_2/Ag_2S/Ag_3PO_4 [11], Ag_3PO_4/Bi_2WO_6 [12], Ag_3PO_4/Cu_2O [13], TiO_2/Ag_3PO_4/bentonite [14], $Co_3(PO_4)_2$/Ag_3PO_4 [15], and Ag_3PO_4/$BiFeO_3$ [16] have been extensively studied due to their excellent photocatalytic activity for photocatalytic degradation of the organic pollutions under visible light irradiation.

Bismuth phosphate ($BiPO_4$) as a photocatalyst has been widely studied because of its good photoelectric performance, low cost, low toxicity, excellent photocatalytic activity, and high

stability [1]. However, the large optical bandgap (E_g = 4.5 eV) of $BiPO_4$ limits the transmission efficiency of photon-generated carriers and light-response range to sunlight [17,18]. To expand the photoresponse range of $BiPO_4$, constructing composite photocatalysts with Ag_3PO_4 (E_g = 2.43 eV) can effectively improve the photocatalytic activity of the composite photocatalysts [19–24]. However, the $Ag_3PO_4/BiPO_4$ photocatalysts have a high recombination rate of photogenerated electrons (e^-) and holes (h^+) in the degradation of organic pollutions in wastewater [25]. To achieve excellent photocatalytic performances of the photocatalysts, the photoexcited electrons and holes must be efficiently separated [26–29].

Noble metal nanoparticles (NPs) and carbon nanomaterials including carbon quantum dots (CQDs), carbon nanotubes (CNTs) and graphene manifest many intriguing physicochemical characteristics and offer a wide scope of technological applications in electronic devices, biomedicine, sensors, and wave absorption [30–37]. These nanomaterials are good carrier transport materials and also exhibit interesting localized surface plasmon resonance (LSPR) effect or photoluminescence (PL) up-conversion effect [38–40]. Due to these outstanding properties, noble metal NPs, CQDs, CNTs, and graphene have been demonstrated to be excellent modifiers or co-catalysts to enhance the photocatalytic performances of semiconductor photocatalysts [41–46].

Herein, we report a hydrothermal synthesis of unique $CQDs/Ag_3PO_4/BiPO_4$ heterostructure photocatalyst. The composite photocatalyst with the CQDs, Ag_3PO_4, and $BiPO_4$ three phase junction structure has not been reported previously and may be commonly applicable to other composite photocatalyst systems. The as-obtained $CQDs/Ag_3PO_4/BiPO_4$ heterostructure photocatalyst possesses a high light absorption capacity, high utilization and separation efficiency of photogenerated carriers, and exhibits a high photocatalytic activity for photocatalytic degradation of the rhodamine B (RhB) dye. The present $CQDs/Ag_3PO_4/BiPO_4$ heterostructure photocatalysts can be used for the design of micro/nano-photocatalytic devices for the wastewater treatment.

2. Materials and Methods

2.1. Synthesis of the Ag_3PO_4 Photocatalyst

According to the formula Ag_3PO_4, an amount of silver nitrate ($AgNO_3$) was mixed with a stoichiometric amount of sodium dihydrogen phosphate (NaH_2PO_4) powder with Ag/P = 3:1 and added into 60 mL distilled water. After that, a stoichiometric amount of ammonium hydroxide ($NH_3{\cdot}H_2O$) was added to the mixture. The whole process was accompanied by magnetic stirring. Subsequently, the above mixture was transferred to a 100 mL high-pressure autoclave and heated to 160 °C for 6 h. After finishing the hydrothermal reaction, the content was taken out and washed with distilled water several times to remove excess alkali ions. The slurry was centrifuged and dried for 12 h at 80 °C to obtain the Ag_3PO_4 photocatalyst. The flow-chart for the synthesis of Ag_3PO_4 photocatalyst via the hydrothermal synthesis method is shown schematically in Figure 1(I).

2.2. Synthesis of the $BiPO_4$ Photocatalyst

According to the formula $BiPO_4$, stoichiometric amounts of bismuth nitrate pentahydrate ($Bi(NO_3)_3{\cdot}5H_2O$), NaH_2PO_4 and $NH_3{\cdot}H_2O$ were successively added in 20 mL of dilute nitric acid solution (2 mL HNO_3 + 18 mL distilled water). The role of HNO_3 is to dissolve $Bi(NO_3)_3{\cdot}5H_2O$. The mixture was filled up to 60 mL by adding distilled water. The remaining experimental steps are consistent with Section 2.1. The flow-chart for the synthesis of $BiPO_4$ photocatalyst via the hydrothermal method is shown schematically in Figure 1(II).

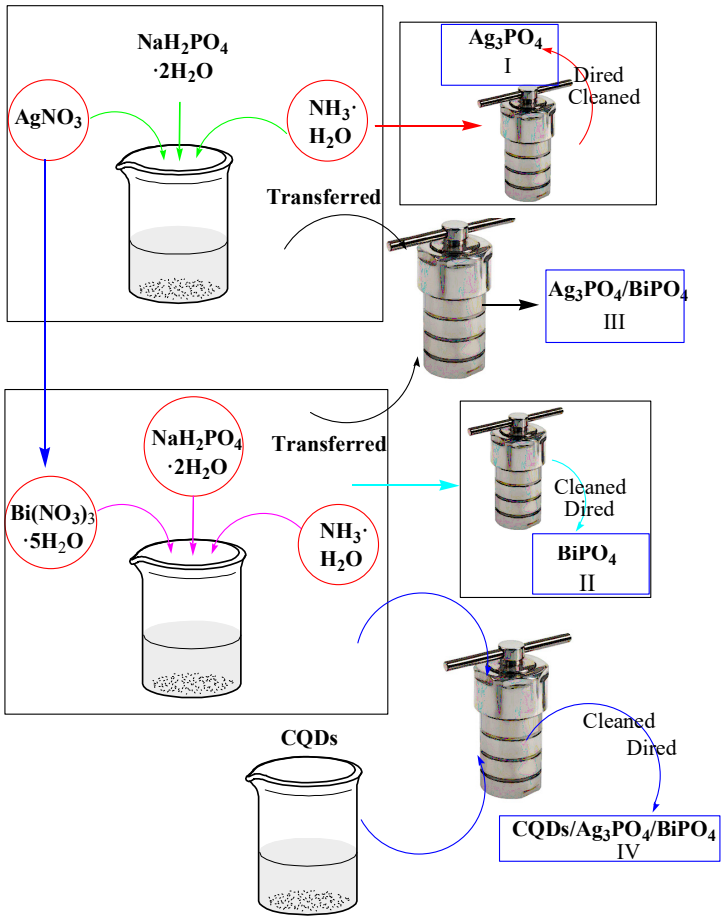

Figure 1. Chemical route for the preparation of (I) Ag_3PO_4, (II) $BiPO_4$, (III) $Ag_3PO_4/BiPO_4$, and (IV) $CQDs/Ag_3PO_4/BiPO_4$.

2.3. Synthesis of $Ag_3PO_4/BiPO_4$ Photocatalyst

To prepare $Ag_3PO_4/BiPO_4$ photocatalyst, stoichiometric amounts of $Bi(NO_3)_3{\cdot}5H_2O$, $AgNO_3$, NaH_2PO_4 and $NH_3{\cdot}H_2O$ (n_{Ag3PO4}:n_{BiPO4} = 1:0.11) were successively added in 20 mL of dilute HNO_3 solution, and then filled up to 60 mL by adding distilled water. The assembly of Ag_3PO_4 on $BiPO_4$ followed the procedure as described in Section 2.1. The flow-chart for the synthesis of the $Ag_3PO_4/BiPO_4$ photocatalyst is schematically shown in Figure 1(III).

2.4. Synthesis of $CQDs/Ag_3PO_4/BiPO_4$ Photocatalyst

To obtain the $CQDs/Ag_3PO_4/BiPO_4$ photocatalyst, stoichiometric amounts of $Bi(NO_3)_3{\cdot}5H_2O$, $AgNO_3$, NaH_2PO_4 and $NH_3{\cdot}H_2O$ and 6 mL of the CQDs suspension derived according the literature [45] were successively 20 mL of dilute HNO_3 solution, and then filled up to 60 mL by adding distilled water. The subsequent preparation process is consistent with Section 2.1. The flow-chart for the synthesis of the $CQDs/Ag_3PO_4/BiPO_4$ photocatalyst is shown in Figure 1(IV).

2.5. Sample Characterization

The phase purity of the Ag_3PO_4, $BiPO_4$, $Ag_3PO_4/BiPO_4$ and $CQDs/Ag_3PO_4/BiPO_4$ photocatalysts was analyzed by means of D8 advanced X-ray diffractometer with Cu Kα radiation at a wavelength of 1.5406 Å. The surface morphology of the samples was characterized by JSM-6701F field-emission scanning electron microscopy (SEM, JEOL Ltd., Tokyo, Japan) and JEM-1200EX field-emission transmission electron microscopy (TEM, JEOL Ltd., Tokyo, Japan). Ultraviolet–visible (UV–VIS) diffuse reflectance spectra of the samples were examined on a UV–VIS spectrophotometer with

an integrating sphere attachment using $BaSO_4$ as the reference. To determine the bonding states, chemical composition, and electron levels of the samples, X-ray photoelectron spectroscopy (XPS) measurements were carried out by using a PHI-5702 X-ray photoelectron spectrometer (Physical Electronics, Hanhassen, MN, USA).

The electrochemical properties of the samples were investigated according to the method reported in the literature [45]. A CST 350 electrochemical workstation (Wuhan Corrtest Instruments Co., Ltd., Wuhan, China) equipped with a three-electrode cell configuration was used to study the electrochemical impedance spectroscopy (EIS) and photocurrent response of the samples. The working electrode was prepared as follows: 15 mg of the photocatalyst, 0.75 mg of polyvinylidene fluoride (PVDF), 0.75 mg of carbon black and 1 mL of 1-methyl-2-pyrrolidione (NMP) were mixed together to form uniform slurry. The slurry mixture was homogeneously coated on the surface of fluorine-doped tin oxide (FTO) thin film (effective area: 1×1 cm^2), and subjected to drying 60 °C for 5 h. The used electrolyte was 0.1 mol L^{-1} Na_2SO_4 aqueous solution. The used light source was a 200 W xenon lamp emitting simulated sunlight. A 0.2 V bias voltage was used during the transient photocurrent measurement. The sinusoidal voltage pulse was used for the EIS measurement (amplitude: 5 mV; frequency range: 10^{-2}–10^5 Hz).

2.6. Photocatalytic Testing

The photocatalytic activities of the samples were investigated by removing RhB from aqueous solution according to the procedure as described in the literature [45]. A 200-W xenon lamp (sunlight simulator) was used as the light source. The photocatalytic system was composed of 0.1 g photocatalyst and 100 mL RhB solution ($C_{photocatalyst}$ = 1 g L^{-1}, C_{RhB} = 5 mg L^{-1}). Based on the initial RhB concentration (C_0) and residual RhB concentration (C_t), the degradation percentage (DP) of RhB was given as: $DP = (C_0 - C_t)/C_0 \times 100\%$.

3. Results and Discussion

3.1. Phase Structural Analysis

Figure 2a,b show the XRD patterns of Ag_3PO_4 and $BiPO_4$, respectively. For the Ag_3PO_4 and $BiPO_4$ samples, the XRD curves were fitted using the Jade 6.0 package. The black curves, red curves, vertical olive lines, and blue lines represent the observed XRD peaks, theoretically estimated curves, Bragg peaks, and difference between the observed values, and theoretically estimated values of XRD diffraction peaks, respectively. The result indicates that the theoretically simulated values are in good agreement with the observed XRD diffraction peaks. The XRD diffraction peaks of Ag_3PO_4 and $BiPO_4$ can be ascribed to JCPDF#06-0505 and JCPDF#15-0767, respectively. Figure 2c shows the XRD patterns of Ag_3PO_4/$BiPO_4$ and CQDs/Ag_3PO_4/$BiPO_4$. The main XRD diffraction peaks of the Ag_3PO_4/$BiPO_4$ and CQDs/Ag_3PO_4/$BiPO_4$ composites are similar to those of pure Ag_3PO_4, indicating that the host lattice of Ag_3PO_4 in these composites undergoes no change. In addition to the XRD characteristic peaks of the Ag_3PO_4 phase, the XRD characteristic peaks of $BiPO_4$ are also observed in these composites. For the CQDs/Ag_3PO_4/$BiPO_4$ composite, the intensity of the diffraction peaks is sharper than that for Ag_3PO_4/$BiPO_4$. The structure analysis shows that the introduction of CQDs in the Ag_3PO_4/$BiPO_4$ composites obviously accelerate the formation of Ag_3PO_4 and $BiPO_4$. In our previous study, the carbon can suppress the formation of M-ferrite [47] and α-Al_2O_3 [48] phase prepared by a polyacrylamide gel method. In this case, this phenomenon may be due to the fact that CQDs do not react with oxygen in the reactor to form carbon dioxide. Figure 2d,e show the crystal structures of $BiPO_4$ and Ag_3PO_4, respectively. The $BiPO_4$ and Ag_3PO_4 are monoclinic phase with space group P21/n (14) and cubic phase with space group P-43n (218), respectively. For the $BiPO_4$, the Bi atom and the P atom are surrounded by eight oxygen atoms and four oxygen atoms, respectively. The wide Bi–O and P–O bond length of $BiPO_4$ exhibits a high photocatalytic activity for photocatalytic degradation of organic pollutants [49]. For the Ag_3PO_4, the Ag atom, P atom and O atom experience four-fold coordination by four O atoms,

four-fold coordination by four O atoms, and 4-fold coordination by one P atom and three Ag atoms, respectively [50].

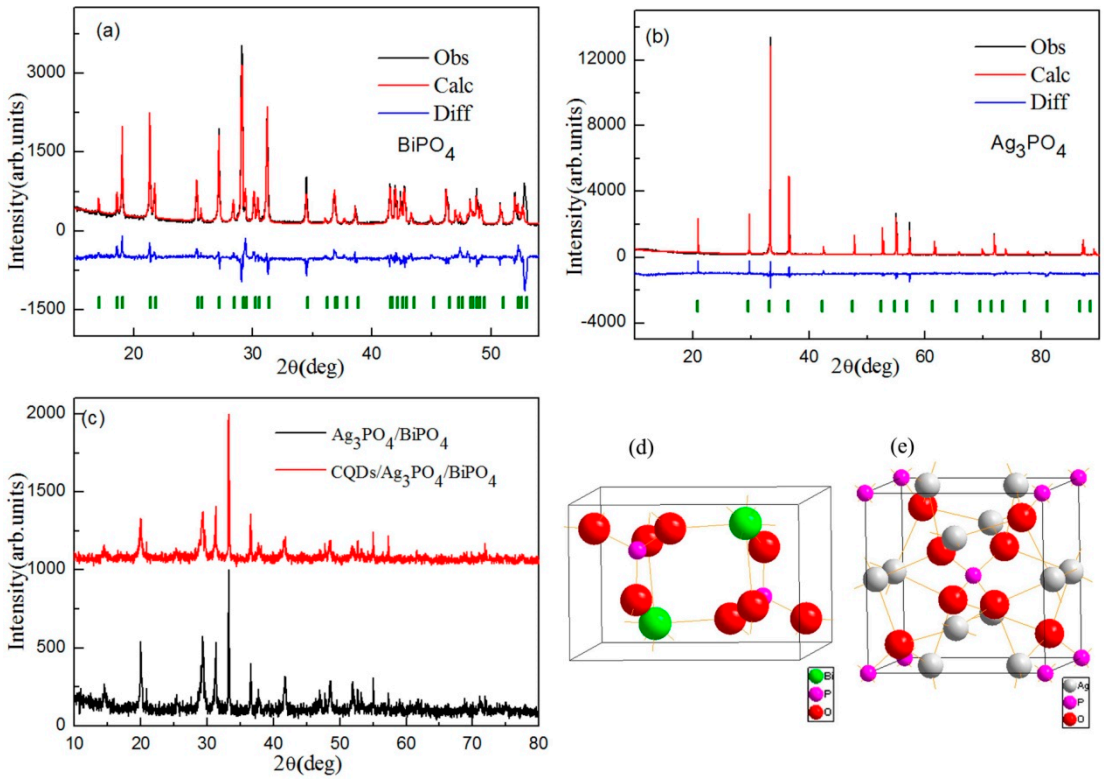

Figure 2. XRD patterns of (**a**) $BiPO_4$, (**b**) Ag_3PO_4, (**c**) $Ag_3PO_4/BiPO_4$ and $CQDs/Ag_3PO_4/BiPO_4$, and crystal structures of (**d**) $BiPO_4$ and (**e**) Ag_3PO_4.

3.2. Surface Morphology and Elemental Component Analysis

Figure 3a,b show the SEM images of $Ag_3PO_4/BiPO_4$ and $CQDs/Ag_3PO_4/BiPO_4$, respectively. For the $Ag_3PO_4/BiPO_4$ composite, the sample is composed of fine spherical particles and rice-like granules, as shown in Figure 3a. Figure 3b represents the SEM image of the $CQDs/Ag_3PO_4/BiPO_4$ composite, revealing that its morphology is very similar to that of the $Ag_3PO_4/BiPO_4$ composite. The insets in Figure 3a,b show the real photos of $Ag_3PO_4/BiPO_4$ and $CQDs/Ag_3PO_4/BiPO_4$, respectively. The results show that the introduction of CQDs to the $Ag_3PO_4/BiPO_4$ composite deepens the color of the sample. The detailed analysis will be done in the optical properties section. Figure 3c shows the SEM image of pure CQDs, from which it is seen that the prepared CQDs have a narrow size distribution of 7–10 nm.

The microstructure and elemental composition of the $CQDs/Ag_3PO_4/BiPO_4$ composite was characterized by TEM, as shown in Figure 4. Figure 4a displays the TEM image of the composite. Spherical fine particles (Ag_3PO_4) are seen to be assembled on the surface of rice-like granules ($BiPO_4$). The high-resolution TEM (HRTEM) image further confirms the assembly of Ag_3PO_4 fine particles on the surface of $BiPO_4$ rice-like granules, as depicted in Figure 4b. The rice-like granules manifest obvious lattice fringes with an interlayer spacing of 0.347 nm, which correspond to the (222) facet of the cubic Ag_3PO_4 phase. The attached spherical particles exhibit the lattice fringes with a d-spacing of 0.407 nm, which correspond to the (101) facet of the monoclinic Ag_3PO_4 phase. The decorated ultrafine particles with no lattice fringes could be CQDs. The energy-dispersive X-ray spectroscopy (EDS) spectrum (Figure 4c) demonstrates that the elemental composition of the $CQDs/Ag_3PO_4/BiPO_4$ composite is Ag, Bi, P, O, and C. Additional Cu signal observed on the EDS spectrum can be ascribed to the TEM microgrid holder [51]. To further elucidate the spatial distribution of elements, Figure 4b shows the dark-field scanning TEM (DF-STEM) image of the $CQDs/Ag_3PO_4/BiPO_4$ composite and Figure 4e–i

display the corresponding elemental maps. Ag, P, O, Bi, and C elementals are homogenously distributed throughout the rice-like granules, implying the uniform decoration of Ag_3PO_4 nanoparticles and CQDs on the surface of rice-like $BiPO_4$ granules. The observed C element in the blank area without the sample could come from the TEM microgrid holder.

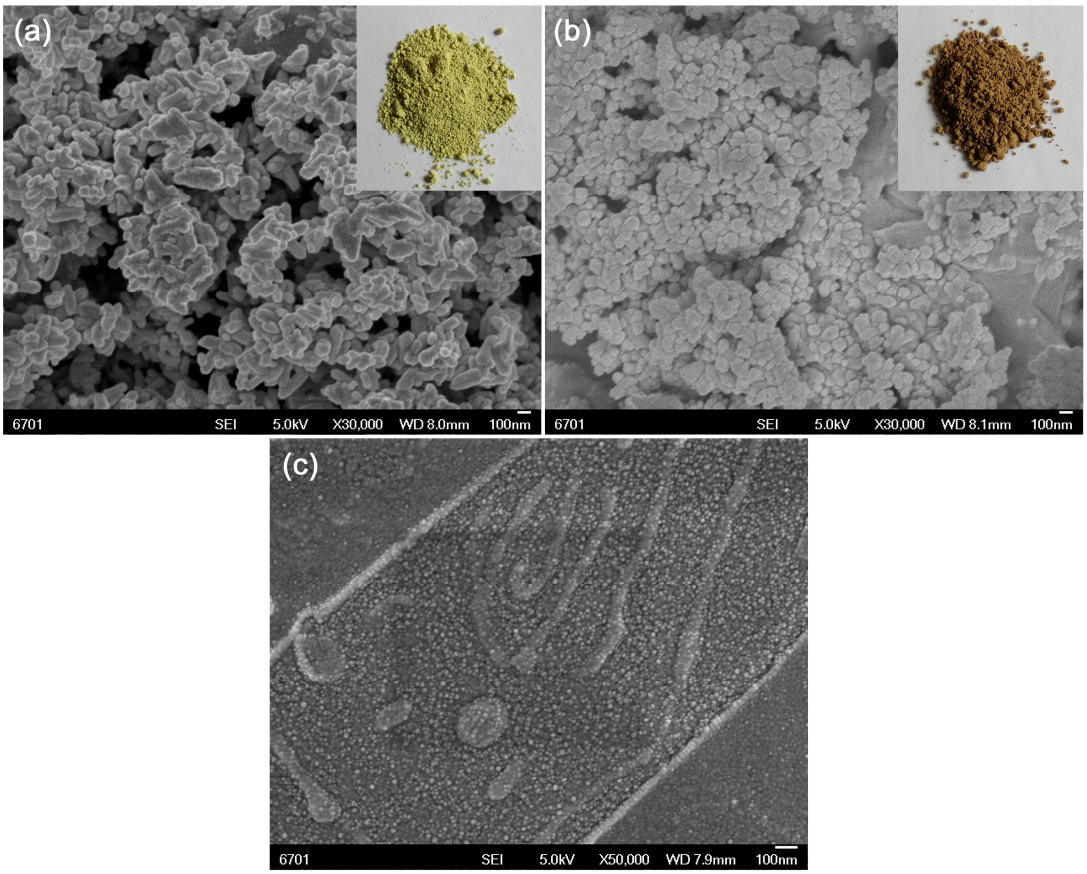

Figure 3. SEM images of (**a**) $Ag_3PO_4/BiPO_4$, (**b**) $CQDs/Ag_3PO_4/BiPO_4$, and (**c**) pure CQDs. The insets represent the real photos of $Ag_3PO_4/BiPO_4$ and $CQDs/Ag_3PO_4/BiPO_4$.

3.3. XPS Analysis

To understand the chemical composition and electronic core levels of the $Ag_3PO_4/BiPO_4$ and $CQDs/Ag_3PO_4/BiPO_4$ composites, Figure 5 shows the XPS results of the two composites. In Figure 5a, the XPS survey scan spectra for the $Ag_3PO_4/BiPO_4$ and $CQDs/Ag_3PO_4/BiPO_4$ composites clearly contain the P, Bi, Ag, O, and C elements. The electronic core levels of Bi 4f, P 2p, Ag 3d, O 1s, and C 1s in the composites are further characterized using the high-resolution XPS spectra. Figure 5b shows the Bi 4f core-level XPS spectra. Two obvious characteristic peaks at 161.02/160.29 and 166.26/165.63 eV are observed on the spectra, which are assigned to Bi $4f_{7/2}$ and Bi $4f_{5/2}$ binding energies of Bi^{3+} in $BiPO_4$, respectively [52].

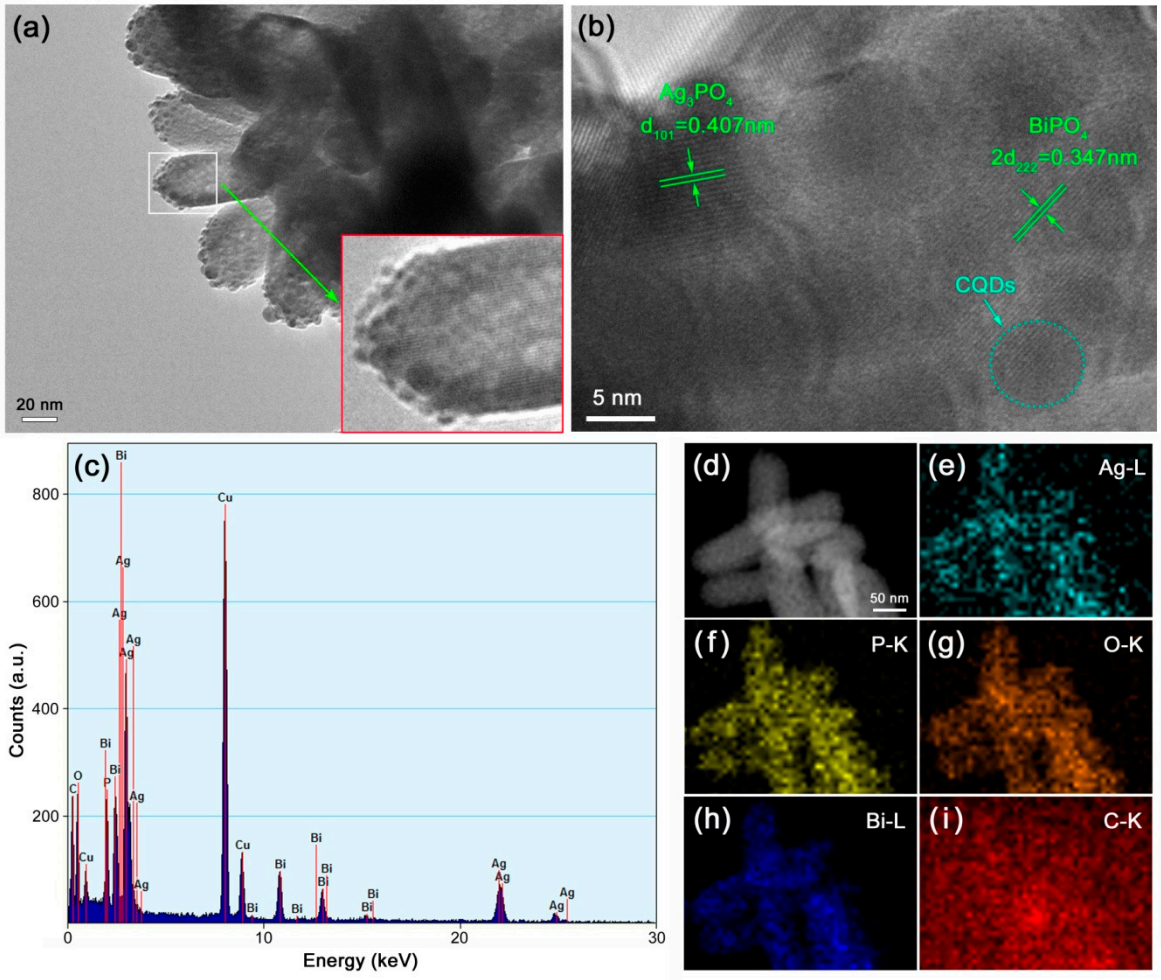

Figure 4. TEM image (**a**), HRTEM image (**b**), EDS spectrum (**c**), DF-STEM image (**d**), and elemental mapping images (**e**–**i**) of the CQDs/Ag_3PO_4/$BiPO_4$ composite.

The XPS spectra of P 2p core level shown in Figure 5c present a broad peak at 134.36 (or 133.69) eV, suggesting that P species exhibits +5 oxidation state [52]. Figure 5d shows the Ag 3d core level XPS spectra. The peaks at 369.59/368.86 and 375.58/374.79 eV can be assigned to Ag $3d_{5/2}$ and Ag $3d_{3/2}$ of Ag_3PO_4, respectively [53]. For the O 1s core-level XPS spectra, the peak at 531.63/532.28 eV can be ascribed to the lattice oxygen, while the peak at 532.92/533.53 eV is related to the adsorbed oxygen [54,55], as shown in Figure 5e. The C 1s core-level XPS spectra are shown in Figure 5f. For the Ag_3PO_4/$BiPO_4$ composite, the peak at 284.77 eV can be assigned to the adventitious hydrocarbon for the XPS instruments [56]. For the CQDs/Ag_3PO_4/$BiPO_4$ composite, the C 1*s* peak can be divided in to three separate peaks at 283.75, 284.77 and 286.38 eV, corresponding to CQDs [57], adventitious hydrocarbon [56] and impurity structure of carbon [58]. It is noted that the electronic core levels of Bi 4f, P 2p, Ag 3d and O 1s for the CQDs/Ag_3PO_4/$BiPO_4$ composite are smaller (about 0.61–0.73 eV) than those for the Ag_3PO_4/$BiPO_4$ composite, which could be due to the fact that the CQDs facilitate the formation of CQDs/Ag_3PO_4/$BiPO_4$ heterostructures.

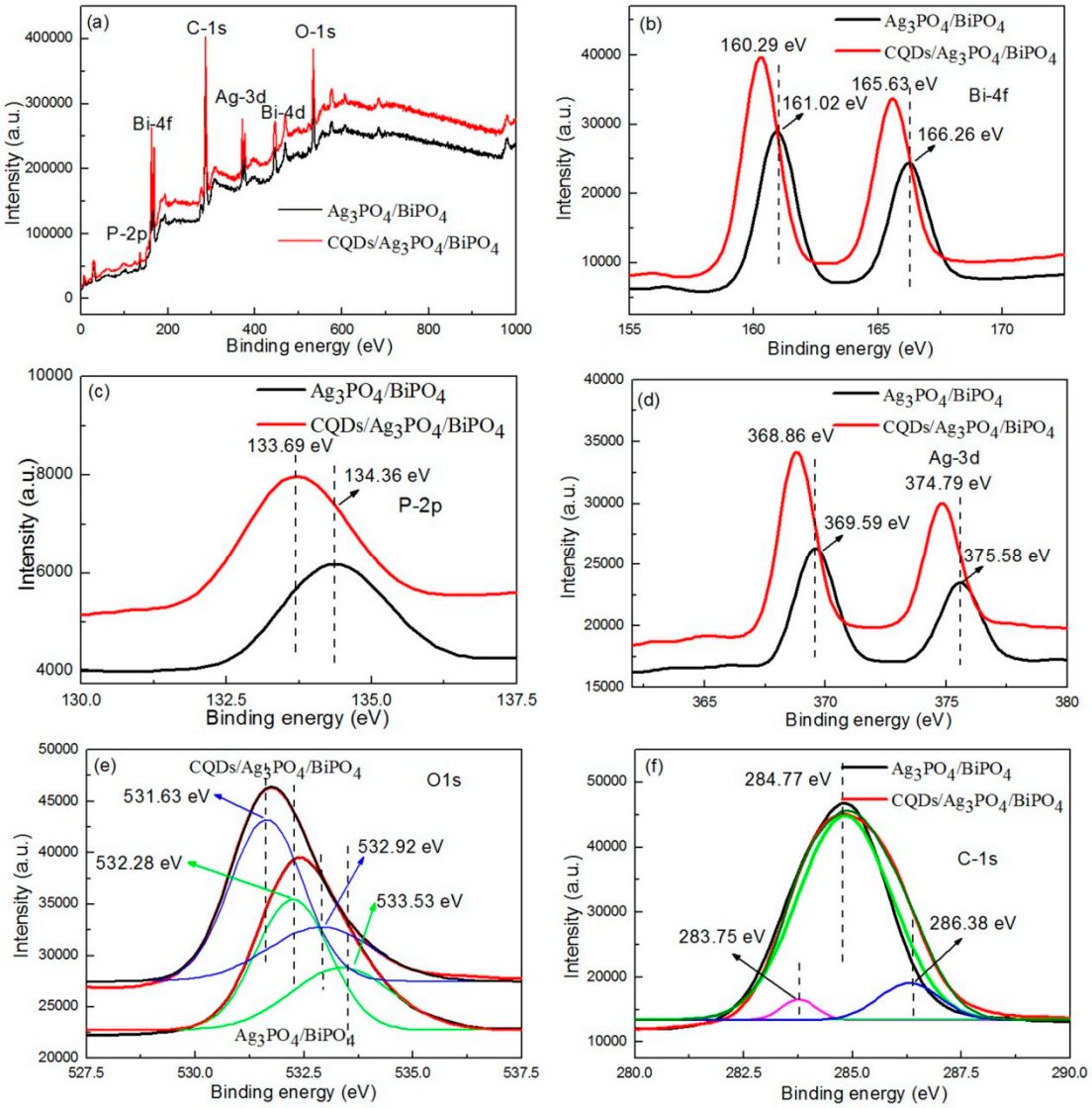

Figure 5. XPS survey scan spectra (**a**), Bi 4f spectra (**b**), P 2p spectra (**c**), Ag 3d spectra (**d**), O 1s spectra (**e**), and C 1s spectra (**f**) of the $Ag_3PO_4/BiPO_4$ and $CQDs/Ag_3PO_4/BiPO_4$ composites.

3.4. Optical Properties

It is noted that the optical properties of semiconductors have an important effect on their photocatalytic performances, which can be determined by UV–vis DRS measurements [59]. Figure 6a shows the UV–VIS diffuse reflectance spectra of the $Ag_3PO_4/BiPO_4$ and $CQDs/Ag_3PO_4/BiPO_4$ photocatalysts. For both the samples, the reflectance first increases and then decreases with the increase in the wavelength, and finally increases again. The two samples present higher reflectance in the wavelength range from 550 to 850 nm. When CQDs are introduced to $Ag_3PO_4/BiPO_4$, a decrease in the reflectance of the resultant $CQDs/Ag_3PO_4/BiPO_4$ composite in the wavelength range from 300 to 850 nm is observed. According to the literatures [60], the color parameters (L^*, a^*, b^*), chroma parameter (c^*), hue angle (H^o), and total color difference (E_{CIE}^*) of $Ag_3PO_4/BiPO_4$ and $CQDs/Ag_3PO_4/BiPO_4$ are evaluated, as shown in Table 1. The $Ag_3PO_4/BiPO_4$ composite shows a negative a* value, indicating that it displays a reseda, as shown in the inset of Figure 3a. The $CQDs/Ag_3PO_4/BiPO_4$ composite exhibits the smaller L^* and b^* values and positive a^* value, which means it exhibits yellowish black, as shown in the inset of Figure 3b. The first derivative curves of UV-vis diffuse reflectance spectra are useful to determine the optical bandgaps (E_g) of semiconductors [61]. As shown in Figure 6b, the $Ag_3PO_4/BiPO_4$

composite shows two absorption edges at 276.1 and 502.3 nm, whereas the CQDs/Ag_3PO_4/$BiPO_4$ composite exhibits an absorption edge at 271.9 nm. The absorption edges at 276.1/271.9 and 502.3 nm can be assigned to $BiPO_4$ and Ag_3PO_4, respectively. The disappearance of the Ag_3PO_4 absorption peak on the spectrum of the CQDs/Ag_3PO_4/$BiPO_4$ composite is ascribed to the enhanced optical absorption caused by CQDs. The E_g values of Ag_3PO_4 and $BiPO_4$ in the samples (see Table 1) can be derived on the basis of Equation (1):

$$E_g(\text{eV}) = \frac{hc}{\lambda_0(\text{nm})} \approx \frac{1240}{\lambda_0(\text{nm})} \quad (1)$$

where λ_0, h, and c is the maximum absorption wavelength, Plank constant, and velocity of light, respectively.

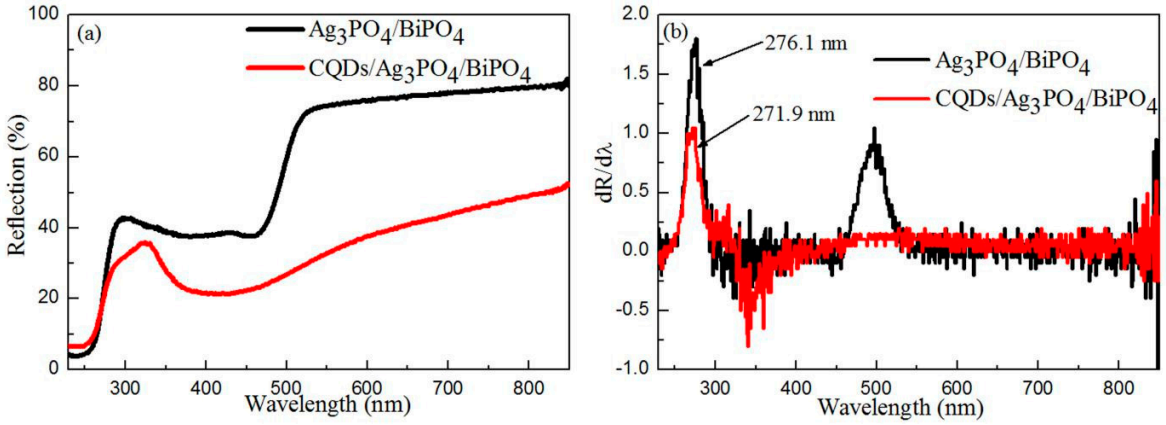

Figure 6. UV–VIS diffuse reflectance spectra (**a**) and the corresponding first derivative curves of the UV–VIS diffuse reflectance spectra (**b**) of the Ag_3PO_4/$BiPO_4$ and CQDs/Ag_3PO_4/$BiPO_4$ composites.

Table 1. Color coordinates and E_g values of Ag_3PO_4/$BiPO_4$ and CQDs/Ag_3PO_4/$BiPO_4$.

Sample	Color Coordinates						E_g of Ag_3PO_4 (eV)	E_g of $BiPO_4$ (eV)
	*L**	*a**	*b**	*c**	*H*°	E_{CIE}*		
Ag_3PO_4/$BiPO_4$	87.110	−3.666	30.235	30.456	−83.087	92.281	2.469	4.491
CQDs/Ag_3PO_4/$BiPO_4$	63.817	4.286	15.421	16.006	74.468	65.794	-	4.561

3.5. Photoelectrochemical Properties

Figure 7a shows the EIS spectra of the Ag_3PO_4/$BiPO_4$ and CQDs/Ag_3PO_4/$BiPO_4$ composites. For the two samples, the EIS spectra show a semicircle and a straight line, which can be ascribed to the charge transfer and the Warburg impedance, respectively [62,63]. The CQDs/Ag_3PO_4/$BiPO_4$ photocatalyst has a smaller semicircle than that for the Ag_3PO_4/$BiPO_4$ photocatalyst, which means the former exhibits a higher photocatalytic activity. Photocurrent response curves can also be used to predict the photocatalytic activity of semiconductor materials [64]. Figure 7b shows the photocurrent response curves of the Ag_3PO_4/$BiPO_4$ and CQDs/Ag_3PO_4/$BiPO_4$ photocatalysts. The photocurrent response of Ag_3PO_4/$BiPO_4$ can be attributed to the electron transfer between Ag_3PO_4 and $BiPO_4$. The CQDs/Ag_3PO_4/$BiPO_4$ photocatalyst exhibits a higher photocurrent intensity than that of Ag_3PO_4/$BiPO_4$, indicating that it possesses a higher photocatalytic activity because of its higher electron transfer and separation efficiency.

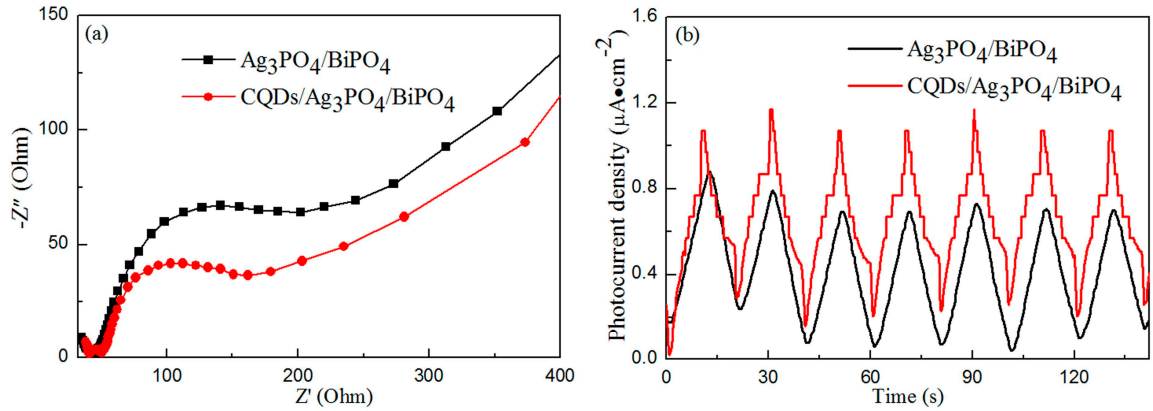

Figure 7. EIS spectra (**a**) and photocurrent response curves (**b**) of the $Ag_3PO_4/BiPO_4$ and $CQDs/Ag_3PO_4/BiPO_4$ composites.

3.6. Photocatalytic Activity

To study the photocatalytic activity of the $BiPO_4$, Ag_3PO_4, $Ag_3PO_4/BiPO_4$, and $CQDs/Ag_3PO_4/BiPO_4$ photocatalysts, RhB dye was used as a degradation dye. Figure 8a shows the time-dependent photodegradation of RhB in the presence of the samples under simulated sunlight irradiation. Based on the blank experiment, the RhB dye exhibits a high stability and is non-biodegradable at ambient conditions. The dye degradation rate over the samples increases with increasing the irradiation time. The photocatalytic activity of these photocatalysts follows the order: $CQDs/Ag_3PO_4/BiPO_4$ > $Ag_3PO_4/BiPO_4$ > Ag_3PO_4 > $BiPO_4$. The result indicates that the $CQDs/Ag_3PO_4/BiPO_4$ composite has the highest photocatalytic activity. It should be noted out that photosensitized degradation of RhB could occur in the present photocatalytic system. However, the photosensitization effect is not the dominant degradation mechanism since Ag_3PO_4 based composite photocatalysts have also been demonstrated to exhibit pronounced degradation of colorless phenol [65].

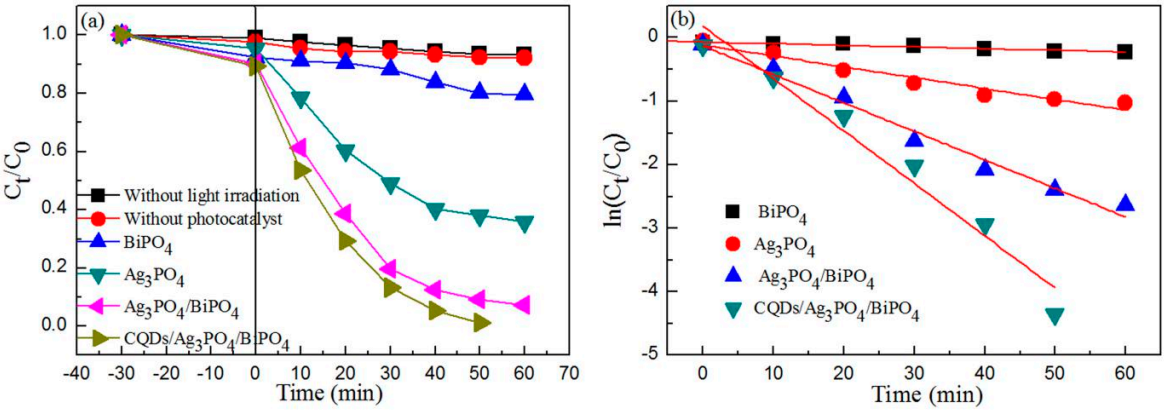

Figure 8. (**a**) Time-dependent photocatalytic degradation of RhB dye over the $BiPO_4$, Ag_3PO_4, $Ag_3PO_4/BiPO_4$, and $CQDs/Ag_3PO_4/BiPO_4$ photocatalysts under simulated sunlight irradiation. (**b**) Plots of $Ln(C/C_0)$ vs. irradiation time for the samples.

The first order kinetic rate of the dye degradation photocatalyzed by the samples can be evaluated by Equation (2) [66]:

$$Ln(C_t/C_0) = -kt \quad (2)$$

where C_0, C_t, k, and t is the initial concentration of RhB, apparent concentration of RhB after degradation, kinetic rate constant, and irradiation time, respectively. Figure 8b shows the plots of $Ln(C_t/C_0)$ vs. t. The rate constant (k) for the photocatalysts is found to be k_{BiPO4} = 0.00261, k_{Ag3PO4} =

0.02853, $k_{Ag3PO4/BiPO4}$ = 0.04489, and $k_{CQDs/Ag3PO4/BiPO4}$ = 0.08259 min^{-1}. The result further indicates that the CQDs/Ag_3PO_4/$BiPO_4$ composite exhibits a photocatalytic activity for the degradation of RhB 31.6, 2.9, and 1.8 times higher than that of $BiPO_4$, Ag_3PO_4 and Ag_3PO_4/$BiPO_4$, respectively. We compare the photodegradation performance of CQDs/Ag_3PO_4/$BiPO_4$ with that of other typical composite photocatalysts, as shown in Table 2. It is seen that the CQDs/Ag_3PO_4/$BiPO_4$ composite photocatalyst prepared in this work manifests a photodegradation performance superior to most of other photocatalysts.

Table 2. Comparison of the photocatalytic performance of CQDs/Ag_3PO_4/$BiPO_4$ with that of previously reported Ag_3PO_4-based composite photocatalysts toward the degradation of RhB.

Samples	Light Source	$C_{photocatalyst}$ (g L^{-1})	C_{RhB} (mg L^{-1})	Irradiation Time (min)	D%	Reference
CQDs/Ag_3PO_4/$BiPO_4$	200 W Xe lamp	1	5	50	98.7	This work
20wt%Ag_3PO_4/Bi_2WO_6	200 W Xe lamp	0.5	5	120	94	[9]
10% $Bi_4Ti_3O_{12}$/Ag_3PO_4	200 W Xe lamp	0.2	5	30	99.5	[6]
Ag-Ag_3PO_4	30 W fluorescent light lamp (λ ≥ 420 nm)	0.75	10	60	70	[67]
Fe_3O_4/ZnO/Ag_3PO_4	50 W LED lamp	0.4	12 (10^{-5} mol/L)	100	75	[68]
15 wt% Ag_3PO_4-Bi_2MoO_6	300 W Xe lamp with a 400-nm cutoff filter	1	10	100	39	[69]
Ag_3PO_4-ZnO (1:40)	300 W Xe lamp with a 400-nm cutoff filter	0.67	12 (10^{-5} mol/L)	30	93	[70]
Ag_3PO_4	15 W four fluorescent lamp	0.3	15	60	75	[71]
AgI/$BiPO_4$	500 W Xe lamp with a 420-nm cutoff filter	1.67	10	60	92.2	[72]
Ag_2S/CQDs/$CuBi_2O_4$	200 W Xe lamp	1	5	60	99.3	[45]
$BiPO_4$/Ag/Ag_3PO_4	150 W Xe lamp with a 420-nm cutoff filter	0.1	20	120	65	[73]

The stability and reusability of the CQDs/Ag_3PO_4/$BiPO_4$ photocatalyst was performed by repeating the experiments for the degradation of the RhB dye under simulated sunlight irradiation, as shown in Figure 9. It is seen that, after five cycles, no obvious decrease in the dye degradation is observed, which indicates that the CQDs/Ag_3PO_4/$BiPO_4$ photocatalyst has a high stability and maintains a high photocatalytic activity for the degradation of RhB.

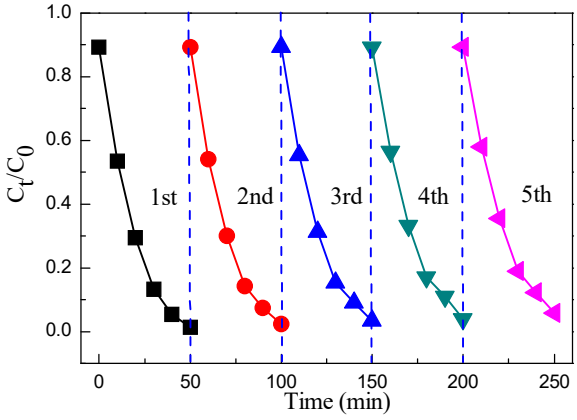

Figure 9. Recyclability of the CQDs/Ag_3PO_4/$BiPO_4$ photocatalyst for the photocatalytic degradation of RhB under simulated sunlight irradiation.

3.7. Photocatalytic Mechanism

Figure 10a schematically shows the assembly structure of the CQDs/Ag_3PO_4/$BiPO_4$ composite with Ag_3PO_4 fine particles and CQDs homogenously decorated on the surface of rice-like $BiPO_4$ granules. A possible photocatalytic mechanism of the CQDs/Ag_3PO_4/$BiPO_4$ composite toward the

degradation of RhB under simulated sunlight irradiation is schematically depicted in Figure 10b. The conduction band (CB) and valence band (VB) potentials of $BiPO_4$ and Ag_3PO_4 can be calculated by using Equations (3) and (4) [74,75]:

$$E_{CB} = X - E^e - 0.5E_g \quad (3)$$

$$E_{VB} = X - E^e + 0.5E_g \quad (4)$$

where E^e is 4.5 eV, being the free electron energy on the hydrogen scale. X_{Ag3PO4} and X_{BiPO4} are estimated as 5.959 and 6.633 eV, respectively, according to Equations (5) and (6):

$$X(Ag_3PO_4) = \sqrt[8]{X(Ag)^3X(P)X(O)^4} \quad (5)$$

$$X(BiPO_4) = \sqrt[6]{X(Bi)X(P)X(O)^4} \quad (6)$$

where X(Ag) = 4.44, X(P) = 5.62, X(Bi) = 4.69, and X(O) = 7.54 eV. The CB potentials of $BiPO_4$ and Ag_3PO_4 are estimated as −0.127, and +0.222 V, respectively, and their corresponding VB potentials are +4.434, and +2.691 V. For the Ag_3PO_4/$BiPO_4$ composite, the energy band of Ag_3PO_4 is completely located within the energy band of $BiPO_4$. Therefore, the Ag_3PO_4/$BiPO_4$ composite obeys the type-I band alignment. When CQDs are introduced to the Ag_3PO_4/$BiPO_4$ composite, it promotes the charge transfer between the two kinds of semiconductors. When the CQDs/Ag_3PO_4/$BiPO_4$ photocatalyst is irradiated by simulated sunlight, the electron transition occurs from the VB to the CB of Ag_3PO_4, thus producing electron-hole pairs. Subsequently, the holes in the VB of Ag_3PO_4 react with the RhB dye to form degradation products. Simultaneously, CQDs can be also excited by absorbing visible light, i.e., the π electrons or σ electrons are excited to the lowest unoccupied molecular orbital (LUMO) [76,77]. The excited CQDs can be acted as excellent electron donors and acceptors. However, $BiPO_4$ could not be photoexcited to generate electron-hole pairs under simulated sunlight irradiation due to its large bandgap energy (4.561 eV). Consequently, the CB electrons in Ag_3PO_4 will transfer to CQDs (π or σ orbitals), and the photoexcited electrons in CQDs will transfer to the CB of $BiPO_4$. Due to this interesting electron transfer process, the recombination of the photoexchited electron-hole pairs in Ag_3PO_4 are efficiently suppressed. Furthermore, the up-conversion photoluminescence emitted from CQDs could excite Ag_3PO_4 to generate additional electron-hole pairs. The photoexcited electrons in the LUMO of CQDs and those relaxed to the CB of $BiPO_4$ react with oxygen in the photocatalytic system to form superoxide ($\bullet O_2^-$) radicals. The produced $\bullet O_2^-$ radicals react with dye molecules adsorbed on the surface of the photocatalyst to produce degradation products.

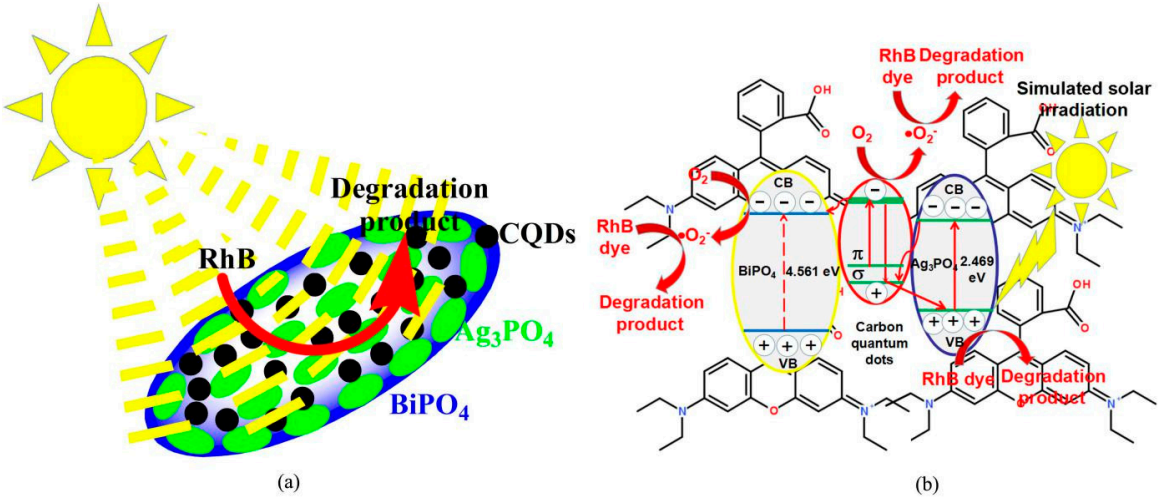

Figure 10. Schematic illustration of the assembly structure (**a**) and a possible photodegradation mechanism (**b**) of the CQDs/Ag_3PO_4/$BiPO_4$ composite.

4. Conclusions

A simple hydrothermal method has been used to synthesize the CQDs/Ag_3PO_4/$BiPO_4$ heterostructure photocatalyst. The carbon quantum dots are anchored at the interfaces between Ag_3PO_4 and $BiPO_4$, thus forming the CQDs/Ag_3PO_4/$BiPO_4$ three-phase junction structure. The three-phase junction structure results in an efficient charge separation and utilization, high light absorption capacity and low photoluminescence intensity. The CQDs/Ag_3PO_4/$BiPO_4$ composite exhibits significantly enhanced photocatalytic activity for the degradation of RhB, which can be explained as the result of efficient charge separation and increased visible-light absorption.

Author Contributions: H.Y. conceived the idea of experiment; H.G. and C.Z. performed the experiments; H.Y., H.G., C.Z., X.N. and S.W. discussed the results; S.W. wrote the manuscript; and all authors read and approved the final manuscript.

Acknowledgments: This work was supported by the National Natural Science Foundation of China (51662027), the Chongqing basic research and frontier exploration (general project) (cstc2019jcyj-msxm1327), the Major Cultivation Projects of Chongqing Three Gorges University (18ZDPY01), the University Scientific Research Project in Gansu Province (2018A-242), and the Study on the Detection of UWB High Range Resolution Radar Target project of the Science and Technology Research Program of the Chongqing Education Commission of China (KJ1601004).

Conflicts of Interest: The authors declare that they have no competing interests.

References

1. Darkwah, W.K.; Adormaa, B.B.; Sandrine, M.K.C.; Ao, Y. Modification strategies for enhancing the visible light responsive photocatalytic activity of the $BiPO_4$ nano-based composite photocatalysts. *Catal. Sci. Technol.* **2019**, *9*, 546–566. [CrossRef]
2. Zhao, X.X.; Yang, H.; Li, S.H.; Cui, Z.M.; Zhang, C.R. Synthesis and theoretical study of large-sized $Bi_4Ti_3O_{12}$ square nanosheets with high photocatalytic activity. *Mater. Res. Bull.* **2018**, *107*, 180–188. [CrossRef]
3. Police, A.K.R.; Vattikuti, S.V.P.; Mandari, K.K.; Chennaiahgari, M.; Sharma, P.; Valluri, D.K.; Byon, C. Bismuth oxide cocatalyst and copper oxide sensitizer in $Cu_2O/TiO_2/Bi_2O_3$ ternary photocatalyst for efficient hydrogen production under solar light irradiation. *Ceram. Int.* **2018**, *44*, 11783–11791. [CrossRef]
4. Vattikuti, S.V.P.; Police, A.K.R.; Shim, J.; Byon, C. In situ fabrication of the Bi_2O_3-V_2O_5 hybrid embedded with graphitic carbon nitride nanosheets: Oxygen vacancies mediated enhanced visible-light-driven photocatalytic degradation of organic pollutants and hydrogen evolution. *Appl. Surf. Sci.* **2018**, *447*, 740–756. [CrossRef]
5. Vattikuti, S.V.P.; Police, A.K.R.; Shim, J.; Byon, C. Visible-Light-Driven photocatalytic activity of SnO_2-ZnO quantum dots anchored on g-C_3N_4 nanosheets for photocatalytic pollutant degradation and H_2 production. *ACS Omega* **2018**, *3*, 7587–7602. [CrossRef]
6. Vattikuti, S.V.P.; Police, A.K.R.; Shim, J.; Byon, C. Sacrifcial-template-free synthesis of core-shell C@Bi_2S_3 heterostructures for efcient supercapacitor and H_2 production applications. *Sci. Rep.* **2018**, *8*, 4194. [CrossRef] [PubMed]
7. He, Z.M.; Tang, B.; Su, J.B.; Xia, Y.M. Fabrication of novel $Cu_2O/Bi_{24}O_{31}Br_{10}$ composites and excellent photocatalytic performance. *J. Mater. Sci. Mater. Electron.* **2018**, *29*, 19544–19553. [CrossRef]
8. Zangeneh, H.; Zinatizadeh, A.A.L.; Habibi, M.; Akia, M.; Isa, M.H. Photocatalytic oxidation of organic dyes and pollutants in wastewater using different modified titanium dioxides: A comparative review. *J. Ind. Eng. Chem.* **2015**, *26*, 1–36. [CrossRef]
9. Zheng, C.X.; Yang, H.; Cui, Z.M.; Zhang, H.M.; Wang, X.X. A novel $Bi_4Ti_3O_{12}/Ag_3PO_4$ heterojunction photocatalyst with enhanced photocatalytic performance. *Nanoscale Res. Lett.* **2017**, *12*, 608. [CrossRef]
10. Wang, X.; Ma, J.; Kong, Y.; Fan, C.; Peng, M.; Komarneni, S. Synthesis of p-n heterojunction $Ag_3PO_4/NaTaO_3$ composite photocatalyst for enhanced visible-light-driven photocatalytic performance. *Mater. Lett.* **2019**, *251*, 192–195. [CrossRef]
11. Liu, Y.; Wang, W.; Si, M.; Zhang, H. Carbon cloth-supported $MoS_2/Ag_2S/Ag_3PO_4$ composite with high photocatalytic activity and recyclability. *ChemCatChem* **2019**, *11*, 1017–1025.
12. Zheng, C.X.; Yang, H. Assembly of Ag_3PO_4 nanoparticles on rose flower-like Bi_2WO_6 hierarchical architectures for achieving high photocatalytic performance. *J. Mater. Sci. Mater. Electron.* **2018**, *29*, 9291–9300. [CrossRef]

13. Naresh, G.; Lee, A.T.; Meena, V.; Satyanarayana, M.; Huang, M.H. Photocatalytic activity suppression of Ag_3PO_4-deposited Cu_2O octahedra and rhombic dodecahedra. *J. Phys. Chem. C* **2019**, *123*, 2314–2320. [CrossRef]
14. Tran, T.T.T.; Doan, V.D.; Ho, T.T.T.; Le, V.T.; Nguyen, H.T. Novel of TiO_2/Ag_3PO_4/bentonite composite photocatalyst: Preparation, characterization, and application for degradation of methylene blue in aqueous solution. *Environ. Eng. Sci.* **2019**, *36*, 71–80. [CrossRef]
15. Geng, Z.; Yang, M.; Qi, X.; Li, Z.; Yang, X.; Huo, M.; Crittenden, J.C. $Co_3(PO_4)_2$/Ag_3PO_4 with enhanced simulated sunlight photocatalytic activity toward ofloxacin degradation and mechanism insight. *J. Chem. Technol. Biotechnol.* **2019**, *94*, 1660–1669. [CrossRef]
16. Di, L.J.; Yang, H.; Xian, T.; Chen, X.J. Facile synthesis and enhanced visible-light photocatalytic activity of novel p-Ag_3PO_4/n-$BiFeO_3$ heterojunction composites for dye degradation. *Nanoscale Res. Lett.* **2018**, *13*, 257. [CrossRef] [PubMed]
17. Lv, Y.; Zhu, Y.; Zhu, Y. Enhanced photocatalytic performance for the $BiPO_{4-x}$ nanorod induced by surface oxygen vacancy. *J. Phys. Chem. C* **2013**, *117*, 18520. [CrossRef]
18. Zhang, Y.; Shen, B.; Huang, H.; He, Y.; Fei, B.; Lv, F. $BiPO_4$/reduced graphene oxidecomposites photocatalyst with high photocatalytic activity. *Appl. Surf. Sci.* **2014**, *319*, 272–277. [CrossRef]
19. Lin, H.; Ye, H.; Xu, B.; Cao, J.; Chen, S. Ag_3PO_4 quantum dot sensitized $BiPO_4$: A novel p–n junction Ag_3PO_4/$BiPO_4$ with enhanced visible-light photocatalytic activity. *Catal. Commun.* **2013**, *37*, 55–59. [CrossRef]
20. Wu, S.; Zheng, H.; Wu, Y.; Lin, W.; Xu, T.; Guan, M. Hydrothermal synthesis and visible light photocatalytic activity enhancement of $BiPO_4$/Ag_3PO_4 composites for degradation of typical dyes. *Ceram. Int.* **2014**, *40*, 14613–14620. [CrossRef]
21. Mohaghegh, N.; Rahimi, E.; Gholami, M.R. Ag_3PO_4/$BiPO_4$ p–n heterojunction nanocomposite prepared in room-temperature ionic liquid medium with improved photocatalytic activity. *Mater. Sci. Semicond. Process.* **2015**, *39*, 506–514. [CrossRef]
22. Mohaghegh, N.; Tasviri, M.; Rahimi, E.; Gholami, M.R. A novel p–n junction Ag_3PO_4/$BiPO_4$-based stabilized Pickering emulsion for highly efficient photocatalysis. *RSC Adv.* **2015**, *5*, 12944–12955. [CrossRef]
23. Li, J.; Yuan, H.; Zhu, Z. In situ growth of Ag_3PO_4 on N-$BiPO_4$ nanorod: A core–shell heterostructure for high performance photocatalyst. *J. Colloid Interface Sci.* **2016**, *462*, 382–388. [CrossRef] [PubMed]
24. Cai, L.; Jiang, H.; Wang, L. Enhanced photo-stability and photocatalytic activity of Ag_3PO_4 via modification with $BiPO_4$ and polypyrrole. *Appl. Surf. Sci.* **2017**, *420*, 43–52. [CrossRef]
25. Mohaghegh, N.; Tasviri, M.; Rahimi, E.; Gholami, M.R. Comparative studies on Ag_3PO_4/$BiPO_4$–metal-organic framework–graphene-based nanocomposites for photocatalysis application. *Appl. Surf. Sci.* **2015**, *351*, 216–224. [CrossRef]
26. Wang, S.Y.; Yang, H.; Wang, X.X.; Feng, W.J. Surface disorder engineering of flake-like Bi_2WO_6 crystals for enhanced photocatalytic activity. *J. Electron. Mater.* **2019**, *48*, 2067–2076. [CrossRef]
27. Wang, S.F.; Gao, H.J.; Wei, Y.; Li, Y.W.; Yang, X.H.; Fang, L.M.; Lei, L. Insight into the optical, color, photoluminescence properties, and photocatalytic activity of the N-O and C-O functional groups decorating spinel type magnesium aluminate. *CrystEngComm* **2019**, *21*, 263–277. [CrossRef]
28. He, Z.M.; Xia, Y.M.; Tang, B.; Jiang, X.F.; Su, J.B. Fabrication and photocatalytic property of ZnO/Cu_2O core-shell nanocomposites. *Mater. Lett.* **2016**, *184*, 148–151. [CrossRef]
29. Zhao, X.X.; Yang, H.; Li, R.S.; Cui, Z.M.; Liu, X.Q. Synthesis of heterojunction photocatalysts composed of Ag_2S quantum dots combined with $Bi_4Ti_3O_{12}$ nanosheets for the degradation of dyes. *Environ. Sci. Pollut. Res.* **2019**, *26*, 5524–5538. [CrossRef]
30. Fernando, K.A.S.; Sahu, S.P.; Liu, Y.; Lewis, W.K.; Guliants, E.; Jafariyan, A.; Wang, P.; Bunker, C.E.; Sun, Y.P. Carbon quantum dots and applications in photocatalytic energy conversion. *ACS Appl. Mater. Interfaces* **2015**, *7*, 8363–8376. [CrossRef]
31. Yi, Z.; Huang, J.; Cen, C.L.; Chen, X.F.; Zhou, Z.G.; Tang, Y.J.; Wang, B.Y.; Yi, Y.G.; Wang, J.; Wu, P.H. Nanoribbon-ring cross perfect metamaterial graphene multi-band absorber in THz range and the sensing application. *Results Phys.* **2019**, *14*, 102367. [CrossRef]
32. Cen, C.L.; Zhang, Y.B.; Liang, C.P.; Chen, X.F.; Yi, Z.; Duan, T.; Tang, Y.J.; Ye, X.; Yi, Y.G.; Xiao, S.Y. Numerical investigation of a tunable dual-band metamaterial perfect absorber consisting of two-intersecting graphene nanorings arrays. *Phys. Lett. A* **2019**, *383*, 3030–3035. [CrossRef]

33. Yi, Z.; Liang, C.P.; Chen, X.F.; Zhou, Z.G.; Tang, Y.J.; Ye, X.; Yi, Y.G.; Wang, J.Q.; Wu, P.H. Dual-band plasmonic perfect absorber based on graphene metamaterials for refractive index sensing application. *Micromachines* **2019**, *10*, 443. [CrossRef] [PubMed]
34. Wang, X.X.; Zhu, J.K.; Tong, H.; Yang, X.D.; Wu, X.X.; Pang, Z.Y.; Yang, H.; Qi, Y.P. A theoretical study of a plasmonic sensor comprising a gold nano-disk array on gold film with an SiO_2 spacer. *Chin. Phys. B* **2019**, *28*, 044201. [CrossRef]
35. Wang, X.X.; Zhu, J.K.; Wen, X.L.; Wu, X.X.; Wu, Y.; Su, Y.W.; Tong, H.; Qi, Y.P.; Yang, H. Wide range refractive index sensor based on a coupled structure of Au nanocubes and Au film. *Opt. Mater. Express* **2019**, *9*, 3079–3088. [CrossRef]
36. Cen, C.L.; Yi, Z.; Zhang, G.F.; Zhang, Y.B.; Liang, C.P.; Chen, X.F.; Tang, Y.J.; Ye, X.; Yi, Y.G.; Wang, J.Q.; et al. Theoretical design of a triple-band perfect metamaterial absorber in the THz frequency range. *Results Phys.* **2019**, *14*, 102463. [CrossRef]
37. Li, M.W.; Liang, C.P.; Zhang, Y.B.; Yi, Z.; Chen, X.F.; Zhou, Z.G.; Yang, H.; Tang, Y.J.; Yi, Y.G. Terahertz wideband perfect absorber based on open loop with cross nested structure. *Results Phys.* **2019**, in press. [CrossRef]
38. Zhang, Y.B.; Cen, C.L.; Liang, C.P.; Yi, Z.; Chen, X.F.; Li, M.W.; Zhou, Z.G.; Tang, Y.J.; Yi, Y.G.; Zhang, G.F. Dual-band switchable terahertz metamaterial absorber based on metal nanostructure. *Results Phys.* **2019**, *14*, 102422. [CrossRef]
39. Wang, X.X.; Bai, X.L.; Pang, Z.Y.; Zhu, J.K.; Wu, Y.; Yang, H.; Qi, Y.P.; Wen, X.L. Surface-enhanced Raman scattering by composite structure of gold nanocube-PMMA-gold film. *Opt. Mater. Express* **2019**, *9*, 1872–1881. [CrossRef]
40. Tong, H.; Xu, Y.Q.; Su, Y.W.; Wang, X.X. Theoretical study for fabricating elliptical subwavelength nanohole arrays by higher-order waveguide-mode interference. *Results Phys.* **2019**, *14*, 102460. [CrossRef]
41. Yan, Y.X.; Yang, H.; Yi, Z.; Li, R.S.; Wang, X.X. Enhanced photocatalytic performance and mechanism of Au@$CaTiO_3$ composites with Au nanoparticles assembled on $CaTiO_3$ nanocuboids. *Micromachines* **2019**, *10*, 254. [CrossRef] [PubMed]
42. Li, T.; Lu, G.; Hu, X.; Xie, W.; Xia, Q.; Luo, S. Ag/Ag_3PO_4/$BiPO_4$ nanocomposites with high photocatalytic degradation activity for 2,4-dichlorophenol. *Mater. Lett.* **2017**, *188*, 392–395. [CrossRef]
43. Di, L.J.; Yang, H.; Xian, T.; Chen, X.J. Construction of Z-scheme g-C_3N_4/CNT/$Bi_2Fe_4O_9$ composites with improved simulated-sunlight photocatalytic activity for the dye degradation. *Micromachines* **2018**, *9*, 613. [CrossRef] [PubMed]
44. Alansi, A.M.; Al-Qunaibit, M.; Alade, I.O.; Qahtan, T.F.; Saleh, T.A. Visible-light responsive BiOBr nanoparticles loaded on reduced graphene oxide for photocatalytic degradation of dye. *J. Mol. Liq.* **2018**, *253*, 297–304. [CrossRef]
45. Gao, H.J.; Wang, F.; Wang, S.F.; Wang, X.X.; Yi, Z.; Yang, H. Photocatalytic activity tuning in a novel Ag_2S/CQDs/$CuBi_2O_4$ composite: Synthesis and photocatalytic mechanism. *Mater. Res. Bull.* **2019**, *115*, 140–149. [CrossRef]
46. Di, L.J.; Xian, T.; Sun, X.F.; Li, H.Q.; Zhou, Y.J.; Ma, J.; Yang, H. Facile preparation of CNT/Ag_2S nanocomposites with improved visible and NIR light photocatalytic degradation activity and their catalytic mechanism. *Micromachines* **2019**, *10*, 503. [CrossRef] [PubMed]
47. Wang, S.F.; Zu, X.T.; Sun, G.Z.; Li, D.M.; He, C.D.; Xiang, X.; Liu, W.; Han, S.B.; Li, S. Highly dispersed spinel (Mg, Ca, Ba)-ferrite nanoparticles: Tuning the particle size and magnetic properties through a modified polyacrylamide gel route. *Ceram. Int.* **2016**, *42*, 19133–19140. [CrossRef]
48. Wang, S.F.; Zhang, C.F.; Sun, G.G.; Yuan, Y.G.; Chen, L.; Xiang, X.; Ding, Q.P.; Chen, B.; Li, Z.J.; Zu, X.T. Self-assembling synthesis of α-Al_2O_3–carbon composites and a method to increase their photoluminescence. *J. Lumin.* **2014**, *153*, 393–400. [CrossRef]
49. Pan, C.; Li, D.; Ma, X.; Chen, Y.; Zhu, Y. Effects of distortion of PO_4 tetrahedron on the photocatalytic performances of $BiPO_4$. *Catal. Sci. Technol.* **2011**, *1*, 1399–1405. [CrossRef]
50. Chen, X.; Dai, Y.; Wang, X. Methods and mechanism for improvement of photocatalytic activity and stability of Ag_3PO_4: A review. *J. Alloys Compd.* **2015**, *649*, 910–932. [CrossRef]
51. Ye, Y.C.; Yang, H.; Zhang, H.M.; Jiang, J.L. A promising Ag_2CrO_4/$LaFeO_3$ heterojunction photocatalyst applied to photo-Fenton degradation of RhB. *Environ. Technol.* **2018**, 1–18. [CrossRef] [PubMed]

52. Li, Z.; Yang, S.; Zhou, J.; Li, D.; Zhou, X.; Ge, C.; Fang, Y. Novel mesoporous g-C_3N_4 and $BiPO_4$ nanorods hybrid architectures and their enhanced visible-light-driven photocatalytic performances. *Chem. Eng. J.* **2014**, *241*, 344–351. [CrossRef]
53. Cruz-Filho, J.F.; Costa, T.M.S.; Lima, M.S.; Silva, L.J.; Santos, R.S.; Cavalcante, L.S.; Longo, E.; Luz, G.E., Jr. Effect of different synthesis methods on the morphology, optical behavior, and superior photocatalytic performances of Ag_3PO_4 sub-microcrystals using white-light-emitting diodes. *J. Photochem. Photobiol. A Chem.* **2019**, *377*, 14–25. [CrossRef]
54. Pooladi, M.; Shokrollahi, H.; Lavasani, S.A.N.H.; Yang, H. Investigation of the structural, magnetic and dielectric properties of Mn-doped $Bi_2Fe_4O_9$ produced by reverse chemical co-precipitation. *Mater. Chem. Phys.* **2019**, *229*, 39–48. [CrossRef]
55. Yan, Y.X.; Yang, H.; Zhao, X.X.; Zhang, H.M.; Jiang, J.L. A hydrothermal route to the synthesis of $CaTiO_3$ nanocuboids using P25 as the titanium source. *J. Electron. Mater.* **2018**, *47*, 3045–3050. [CrossRef]
56. Wang, S.F.; Zhang, C.F.; Sun, G.G.; Chen, B.; Xiang, X.; Wang, H.; Fang, L.M.; Tian, Q.; Ding, Q.P.; Zu, X.T. Fabrication of a novel light emission material $AlFeO_3$ by a modified polyacrylamide gel route and characterization of the material. *Opt. Mater.* **2013**, *36*, 482–488. [CrossRef]
57. Gupta, A.; Verma, N.C.; Khan, S.; Nandi, C.K. Carbon dots for naked eye colorimetric ultrasensitive arsenic and glutathione detection. *Biosens. Bioelectron.* **2016**, *81*, 465–472. [CrossRef]
58. Munoz-Sandoval, E.; Cortes-Lopez, A.J.; Flores-Gomez, B.; Fajardo-Diaz, J.L.; Sanchez-Salas, R.; Lopez-Urias, F. Carbon sponge-type nanostructures based on coaxial nitrogen-doped multiwalled carbon nanotubes grown by CVD using benzylamine as precursor. *Carbon* **2017**, *115*, 409–421. [CrossRef]
59. Wang, X.X.; Pang, Z.Y.; Yang, H.; Qi, Y.P. Theoretical study of subwavelength circular grating fabrication based on continuously exposed surface plasmon interference lithography. *Results Phys.* **2019**, *14*, 102446. [CrossRef]
60. Gao, H.; Yang, H.; Wang, S.; Zhao, X. Optical and electrochemical properties of perovskite type $MAlO_3$ (M=Y, La, Ce) pigments synthesized by a gamma-ray irradiation assisted polyacrylamide gel route. *Ceram. Int.* **2018**, *44*, 14754–14766. [CrossRef]
61. Zhao, X.X.; Yang, H.; Zhang, H.M.; Cui, Z.M.; Feng, W.J. Surface-disorder-engineering-induced enhancement in the photocatalytic activity of $Bi_4Ti_3O_{12}$ nanosheets. *Desalin. Water Treat.* **2019**, *145*, 326–336. [CrossRef]
62. Yan, Y.X.; Yang, H.; Yi, Z.; Xian, T.; Wang, X.X. Direct Z-scheme $CaTiO_3$@BiOBr composite photocatalysts with enhanced photodegradation of dyes. *Environ. Sci. Pollut. Res.* **2019**, 1–12. [CrossRef] [PubMed]
63. Xia, Y.M.; He, Z.M.; Su, J.B.; Hu, K.J. Construction of novel Cu_2O/$PbBiO_2Br$ composites with enhanced photocatalytic activity. *J. Mater. Sci. Mater. Electron.* **2019**, *30*, 9843–9854. [CrossRef]
64. Zhao, X.X.; Yang, H.; Cui, Z.M.; Yi, Z.; Yu, H. Synergistically enhanced photocatalytic performance of $Bi_4Ti_3O_{12}$ nanosheets by Au and Ag nanoparticles. *J. Mater. Sci. Mater. Electron.* **2019**, *30*, 13785–13796. [CrossRef]
65. Raizadaa, P.; Sudhaik, A.; Singh, P.; Shandilya, P.; Gupta, V.K.; Hosseini-Bandegharaei, A.; Agrawal, S. Ag_3PO_4 modified phosphorus and sulphur co-doped graphitic carbon nitride as a direct Z-scheme photocatalyst for 2, 4-dimethyl phenol degradation. *J. Photochem. Photobiol. A Chem.* **2019**, *374*, 22–35. [CrossRef]
66. Xia, Y.M.; He, Z.M.; Hu, K.J.; Tang, B.; Su, J.B.; Liu, Y.; Li, X.P. Fabrication of n-$SrTiO_3$/p-Cu_2O heterojunction composites with enhanced photocatalytic performance. *J. Alloys Compd.* **2018**, *753*, 356–363. [CrossRef]
67. Lei, Y.; Wang, G.; Guo, P.; Song, H.C. Silver phosphate based plasmonic photocatalyst: Highly active visible-light-enhanced photocatalytic property and photosensitized degradation of pollutants. *Funct. Mater. Lett.* **2012**, *5*, 1250047. [CrossRef]
68. Shekofteh-Gohari, M.; Habibi-Yangjeh, A. Photosensitization of Fe_3O_4/ZnO by AgBr and Ag_3PO_4 to fabricate novel magnetically recoverable nanocomposites with significantly enhanced photocatalytic activity under visible-light irradiation. *Ceram. Int.* **2016**, *42*, 15224–15234. [CrossRef]
69. Du, X.; Wan, J.; Jia, J.; Pan, C.; Hu, X.; Fan, J.; Liu, E. Photocatalystic degradation of RhB over highly visible-light-active Ag_3PO_4-Bi_2MoO_6 heterojunction using H_2O_2 electron capturer. *Mater. Des.* **2017**, *119*, 113–123. [CrossRef]
70. Dong, C.; Wu, K.L.; Li, M.R.; Liu, L.; Wei, X.W. Synthesis of Ag_3PO_4–ZnO nanorod composites with high visible-light photocatalytic activity. *Catal. Commun.* **2014**, *46*, 32–35. [CrossRef]

71. Vu, T.A.; Dao, C.D.; Hoang, T.T.T.; Nguyen, K.T.; Le, G.H.; Dang, P.T.; Tran, H.T.K.; Nguyen, T.V. Highly photocatalytic activity of novel nano-sized Ag_3PO_4 for Rhodamine B degradation under visible light irradiation. *Mater. Lett.* **2013**, *92*, 57–60. [CrossRef]
72. Ye, H.; Lin, H.; Cao, J.; Chen, S.; Chen, Y. Enhanced visible light photocatalytic activity and mechanism of $BiPO_4$ nanorods modified with AgI nanoparticles. *J. Mol. Catal. A Chem.* **2015**, *397*, 85–92. [CrossRef]
73. Mohaghegh, N.; Rahimi, E. $BiPO_4$ photocatalyst employing synergistic action of Ag/Ag_3PO_4 nanostructure and graphene nanosheets. *Solid State Sci.* **2016**, *56*, 10–15. [CrossRef]
74. Wang, S.F.; Gao, H.J.; Fang, L.M.; Wei, Y.; Li, Y.W.; Lei, L. Synthesis and characterization of $BaAl_2O_4$ catalyst and its photocatalytic activity towards degradation of methylene blue dye. *Z. Phys. Chem.* **2018**, *233*, 1161–1181. [CrossRef]
75. Di, L.J.; Yang, H.; Xian, T.; Liu, X.Q.; Chen, X.J. Photocatalytic and photo-Fenton catalytic degradation activities of Z-scheme $Ag_2S/BiFeO_3$ heterojunction composites under visible-light irradiation. *Nanomaterials* **2019**, *9*, 399. [CrossRef] [PubMed]
76. Li, H.T.; Kang, Z.H.; Liu, Y.; Lee, S.T. Carbon nanodots: Synthesis, properties and applications. *J. Mater. Chem.* **2012**, *22*, 24230–24253. [CrossRef]
77. Wang, S.Y.; Yang, H.; Yi, Z.; Wang, X.X. Enhanced photocatalytic performance by hybridization of Bi_2WO_6 nanoparticles with honeycomb-like porous carbon skeleton. *J. Environ. Manag.* **2019**, *248*, 109341. [CrossRef]